

LaneAF: Robust Multi-Lane Detection with Affinity Fields

Hala Abualsaud[†], Sean Liu[†], David Lu[†], Kenny Situ[†], Akshay Rangesh[†], and Mohan M. Trivedi

Laboratory for Intelligent & Safe Automobiles, UC San Diego

{habualsa, sel118, dblu, ksitu, arangesh, mtrivedi}@ucsd.edu

Abstract—This study presents an approach to lane detection involving the prediction of binary segmentation masks and per-pixel affinity fields. These affinity fields, along with the binary masks, can then be used to cluster lane pixels horizontally and vertically into corresponding lane instances in a post-processing step. This clustering is achieved through a simple row-by-row decoding process with little overhead; such an approach allows LaneAF to detect a variable number of lanes without assuming a fixed or maximum number of lanes. Moreover, this form of clustering is more interpretable in comparison to previous visual clustering approaches, and can be analyzed to identify and correct sources of error. Qualitative and quantitative results obtained on popular lane detection datasets demonstrate the model’s ability to detect and cluster lanes effectively and robustly. Our proposed approach performs on par with state-of-the-art approaches on the limited TuSimple benchmark, and sets a new state-of-the-art on the challenging CULane dataset.

I. INTRODUCTION

Lane detection is the process of automatically perceiving the shape and position of marked lanes and is a crucial component of autonomous driving systems, directly influencing the guidance and steering of vehicles while also aiding the interaction between numerous agents on the road. As the number of drivers on the roads has increased, autonomous driving systems have received considerable attention in the automotive and tech industries as well as in academia [1]. According to the Insurance Institute for Highway Safety (IIHS), in the US alone, car accidents claimed 36,560 lives in 2018, underscoring the importance of any technology that can help prevent crashes.

Since roads commonly have different types of lane lines (solid white, broken white, solid yellow, etc.), each of which have specific implications with regards to how vehicles may interact with them, automated lane detection systems can also help alert drivers when there are changes in lane topology on the road. Furthermore, there are several factors that make lane detection a challenging task. Firstly, there is a wide variety of road infrastructure in use around the world. Additionally, the lane detection system must be able to identify instances where lanes are ending, merging, and splitting. Finally, the lane detection system must possess the ability to discern worn or unclear lane markings. Precise detection

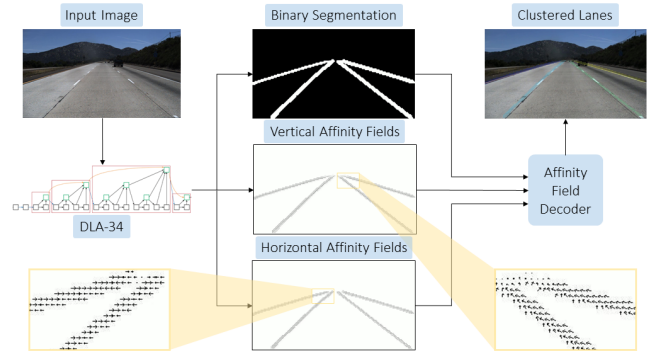


Fig. 1: In our approach, we propose to train a model that outputs binary segmentation masks and affinity fields, which can then be decoded together to produce multiple lane instances. This is opposed to the standard approach to (anchor-free) lane detection that treats each lane as a separate class and trains a model to perform multi-class segmentation.

of lanes also enable more robust trajectory prediction of surrounding vehicles; as discussed in [2], this is critical for successful path planning in autonomous driving. Therefore, while lane detection is a significant and complex task, it is a key factor in developing any autonomous vehicle system.

While binary classification is used for the detection of lanes in our approach, a limitation of this type of classification is that it produces a single-channel output, which does not allow for the identification of separate lane entities. To dissociate different lane instances, we propose a novel clustering scheme based on affinity fields (see Figure 1). Affinity fields were originally introduced in [3] for the purpose of multi-person 2D pose estimation, and are comprised of unit vectors that encode location and orientation. This technique was also used for the detection of hands inside a vehicle, as demonstrated in [4]. In this paper, we have defined two types of affinity fields, the horizontal affinity field (HAF) and vertical affinity field (VAF). It is these affinity fields that enable unique lane instances to be identified and segmented. Since these affinity fields are present wherever there are foreground lane pixels, they are not bound to a pre-determined number of lanes. The model is therefore agnostic to the number of lanes present on the road.

The main contributions of this paper are as follows:

- 1) We show that using an off-the-shelf convolutional neural network (CNN) backbone [5] that intrinsically aggregates and refines multi-scale features can result in

[†]authors contributed equally

Code: <https://github.com/sel118/LaneAF>

The authors are with the Laboratory for Intelligent and Safe Automobiles at the University of California, San Diego, CA 92092, USA.

email: {habualsa, sel118, dblu, ksitu, arangesh, mtrivedi}@ucsd.edu

superior performance when compared to other bespoke architectures and losses previously proposed for lane detection.

- 2) We propose affinity fields that are suitable for clustering and associating pixels belonging to amorphous entities like lanes.
- 3) We detail the procedure and losses to train models that predict binary segmentation masks and affinity fields for the purpose of lane instance segmentation.
- 4) We introduce efficient methods for generating and decoding such affinity fields into an unknown number of clustered lane instances.

II. RELATED RESEARCH

Lane detection has traditionally been tackled by feature-based approaches which then evolved to model-based approaches to detect lane boundaries. However, these are not practical in real world scenarios since they require ideal road scenes to work effectively. Currently, data-driven approaches are commonly used to detect both lane boundaries as well as lane regions. While several shortcomings of the traditional lane detection methods (i.e. lane segmentation via hand-crafted features) have been resolved with more robust methods in recent years, there is still room for improvement. In more recent times, deep learning and large-scale datasets have provided solutions to many of these issues. However, lane detection in unconstrained environments and complex scenarios remain a challenge.

Lane detection nowadays is typically modelled as a semantic segmentation problem to extract features using deep learning methods. New approaches tackle lane detection as a multi-class segmentation problem, where each lane forms a separate class. Some of these approaches include: [6], [7], [8], [9], and [10]. In [8], the authors combine a recurrent neural network (RNN) with a CNN for lane prediction and detection. The use of an embedding loss was introduced in [9] which uses generative adversarial networks (GANs) to better preserve the structure of lanes and to mitigate the problem of complex post-processing for the output of semantic segmentation; 96% accuracy on the TuSimple dataset was obtained. In [10], a sequential prediction network has been used to avoid heuristic-based clustering post-processing. Another network architecture was presented in [11] with two elements: a deep network which generates weighted pixel coordinates in addition to a differentiable weighted least-squares fitting module. In [12], the authors introduced Self Attention Distillation (SAD) loss to avoid models that propagate data sequentially and to decrease inference time. However, the fully connected layer that the SAD model employs is computationally expensive and cannot adapt to any number of lanes.

Other lane detection approaches choose to first perform binary segmentation of all lanes, followed by a clustering stage to separate each individual lane instance as in [13], [14], and [15]. Lane detection is posed as an instance segmentation problem in [13] so that each lane can be detected in an end-to-end manner, adapting to changing numbers

of lanes on the road. In [14], a combination of instance segmentation and classification was used as an end-to-end deep learning real-time method to avoid reliance on two-step detection networks. Although recent methods of lane detection show high accuracy when applied to the popular published datasets, some drawbacks of these current methods are that they are not robust when encountering occlusion and that they require a fixed number of lanes in a scene; thus, they cannot work for a random number of lanes present on the road. Acknowledging this problem is [15], which uses a key points estimation approach to allow for lane detection of an arbitrary numbers of lanes regardless of orientation.

More recently, some approaches have modelled lane detection as an anchor-based object detection problem such as [16], [17], [18], and [19]. One of the approaches that aimed to enhance lane estimation was to use contextual cues to improve computational efficiency and accuracy of lane detection [19]. The authors in [20] introduced a spatial CNN with learned spatial kernels. This method has improved performance over conventional CNN methods since it provides spatial information by computing slice by slice convolution in feature maps, enabling information to be transferred between pixels within each layer. In [18], a spatio-temporal deep learning method was proposed to mitigate the errors that can occur when experiencing harsh weather or other complex problems in the road, jeopardizing the accuracy of detecting a lane in the scene. Meanwhile, in [16], lane markers were tracked temporally. Additionally, [21] presents an anchor-based single-stage deep lane detection model using anchors for feature pooling. In [17], the authors developed 3D-LaneNet, a network that predicts the 3D layout of lanes using a single image. A combination of LiDAR and camera sensors were used in [22] for their network to obtain accurate lane detection in 3D space directly.

The methods in this paper were inspired by [3], which presented an approach to 2D pose estimation of multiple people in an image through Part Affinity Fields (PAFs). The technique introduced takes an input image, passes it to a two-branch CNN, obtains the confidence maps to detect body parts, utilizes PAFs for parts association, parses using a greedy algorithm, and finally assembles them into the final image with estimated poses. The main takeaway from [3] is that parsing based on PAFs adds robustness with regards to part detection and association.

III. METHODOLOGY

Our proposed methodology involves a feed-forward CNN that is trained to predict binary lane segmentation masks and per-pixel affinity fields. More specifically, the model is trained to predict two affinity fields, which we call the horizontal affinity field (HAF) and vertical affinity field (VAF), respectively. Affinity fields can be thought of as vector fields that map any 2D location on the image plane to a unit vector in 2D. A unit vector in the VAF encodes the direction in which the next set of lane pixels above it is located. On the other hand, a unit vector in the HAF points toward the center of the lane in the current row - thereby allowing us

Algorithm 1 Creating affinity fields from ground truth data

Inputs:
 $SEG(H \times W)$: ground truth segmentation
 l_{max} : maximum number of lanes

$HAF, VAF \leftarrow zeros(H, W, 2)$ \triangleright initialize affinity fields
for $l \leftarrow 1$ **to** L **do** \triangleright go through each lane
 $prev_cols \leftarrow nonzero(SEG[H, :] == l)$ \triangleright initialize
 / row-by-row, from bottom to top */*
 for $y \leftarrow H - 1$ **to** 1 **do**
 $cols \leftarrow find(SEG[row, :] == l)$ \triangleright find lane pixels
 / horizontal affinity field */*
 for x **in** $cols$ **do**
 $HAF[y, x] \leftarrow \vec{H}_{gt}(x, y)$ \triangleright Eq. 1
 end for
 / vertical affinity field */*
 for x **in** $prev_cols$ **do**
 $HAF[y + 1, x] \leftarrow \vec{V}_{gt}(x, y + 1)$ \triangleright Eq. 2
 end for
 $prev_cols \leftarrow cols$
 end for
end for
return HAF, VAF

to cluster lanes of arbitrary widths. These two affinity fields in conjunction with the predicted binary segmentation can then be used to cluster foreground pixels into lanes as a post-processing step. In the next few subsections, we discuss each individual block in our proposed approach.

A. Network Backbone

Recent lane detection approaches have made use of a variety of backbone architectures; but most popular among them are usually the ResNet family of architectures [23], ENet [6], and ERFNet [24]. Although these architectures have proven benefits across a variety of tasks, we believe that more recent developments in the field can be leveraged for the purpose of lane detection. To this end, we make use of the DLA-34 backbone presented in [5].

The DLA family of models make use of deep layer aggregation, which unifies semantic and spatial fusion for better localization and semantic interpretation. In particular, this architecture extends densely connected networks [25] and feature pyramid networks with hierarchical and iterative skip connections that deepen the representation and refine resolution. They employ two forms of aggregation: iterative deep aggregation (IDA) and hierarchical deep aggregation (HDA). IDA focuses on fusing resolutions and scales while HDA focuses on merging features from all modules and channels. These architectures also incorporate deformable convolution operations [26] that can adapt the spatial sampling grid for convolutions based on their inputs. We believe these are desirable properties for the tasks of lane detection and instance segmentation.

B. Affinity Fields

In addition to binary lane segmentation masks, our model is trained to predict horizontal and vertical affinity fields (HAFs and VAFs respectively). For any given image, the

Algorithm 2 Decoding predicted affinity fields into lanes

Inputs:
 $BW(H \times W)$: binary segmentation mask
 $HAF(H \times W \times 2)$: horizontal affinity field
 $VAF(H \times W \times 2)$: vertical affinity field
 τ : clustering threshold

$SEG \leftarrow zeros(H, W)$ \triangleright initialize segmentation output
 $lane_end_points \leftarrow []$
 \triangleright keeps track of the latest points added to each lane
 $L \leftarrow 0$ \triangleright initialize number of lanes to 0
/ row-by-row, from bottom to top */*
for $y \leftarrow H$ **to** 1 **do**
 $cols \leftarrow find(BW[row, :] > 0)$ \triangleright find foreground pixels
 / cluster horizontally */*
 $clusters \leftarrow []$
 for x **in** $cols$ **do**
 $clusters.update(c_{haf}^*(x, y))$ \triangleright Eq. 3
 end for
 / assign clusters to existing lanes */*
 for $l \leftarrow 1$ **to** L **do**
 if $d^*(l) \leq \tau$ **then** \triangleright error less than threshold (Eq. 5)
 $lane_end_points[l] \leftarrow c_{haf}^*(l)$ \triangleright Eq. 4, Eq. 6
 \triangleright update latest points added to lane
 for x **in** $c_{haf}^*(l)$ **do**
 $SEG[y, x] \leftarrow l$ \triangleright assign cluster to lane l
 end for
 end if
 end for
 / spawn new lanes with unassigned clusters */*
 for $cluster$ **in** $clusters$ **do**
 if $cluster$ **is not assigned** **then**
 $L \leftarrow L + 1$
 $lane_end_points[L] \leftarrow cluster$
 end if
 end for
end for
return SEG

HAF and VAF can be thought of as vector fields $\vec{H}(\cdot, \cdot)$ and $\vec{V}(\cdot, \cdot)$, that assign a unit vector to each (x, y) location in the image. As we alluded to earlier, the HAF enables us to cluster lane pixels horizontally and the VAF vertically. With the predicted affinity fields and binary mask, clustering lane pixels is achieved through a simple row-by-row decoding process from bottom to top. The rest of this subsection provides details on how to create such affinity fields using the ground truth and how to use the predicted affinity fields to decode individual lanes.

Creating HAFs and VAFs: Affinity fields are created using ground truth segmentation masks on the fly as detailed in Algorithm 1. This proceeds row-by-row, from bottom to top.

For any row y in the image, the HAF vectors are computed for each lane point (x_i^l, y) using the ground truth vector field mapping $\vec{H}_{gt}(\cdot, \cdot)$ as follows:

$$\begin{aligned} \vec{H}_{gt}(x_i^l, y) &= \left(\frac{\bar{x}_y^l - x_i^l}{|\bar{x}_y^l - x_i^l|}, \frac{y - y}{|y - y|} \right)^\top \\ &= \left(\frac{\bar{x}_y^l - x_i^l}{|\bar{x}_y^l - x_i^l|}, 0 \right)^\top, \end{aligned} \quad (1)$$

where \bar{x}_y^l is the mean x -coordinate of all points belonging

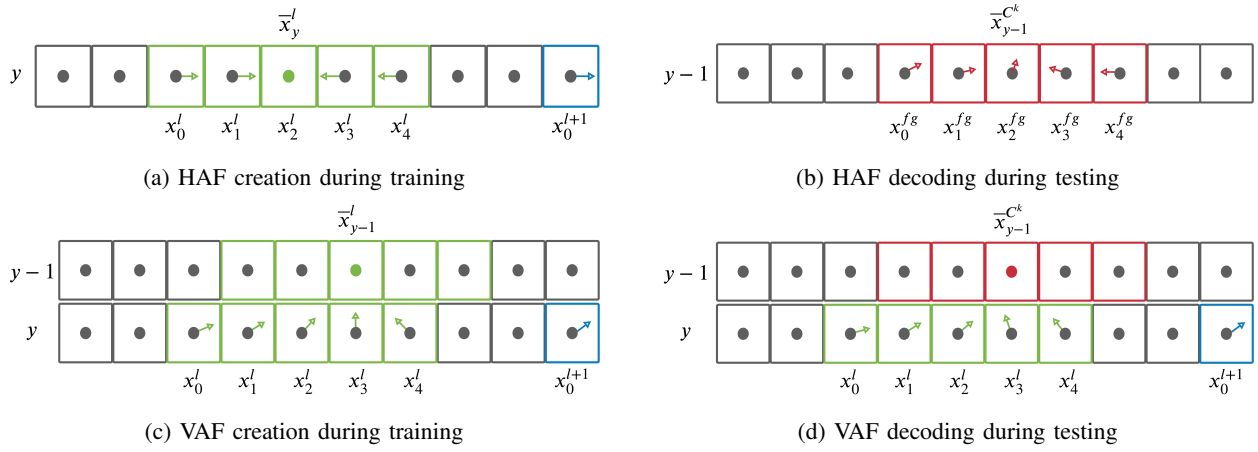


Fig. 2: Illustrations of HAF and VAF creation and decoding processes during training and testing, respectively.

to lane l in row y . This process is illustrated in Figure 2a, where pixels in green and blue represent points belonging to lanes l and $l + 1$ respectively.

Similarly, the VAF vectors are computed for each lane point (x_i^l, y) in row y using the ground truth vector field mapping $\vec{V}_{gt}(\cdot, \cdot)$ as follows:

$$\begin{aligned} \vec{V}_{gt}(x_i^l, y) &= \left(\frac{\bar{x}_{y-1}^l - x_i^l}{|\bar{x}_{y-1}^l - x_i^l|}, \frac{y-1-y}{|y-1-y|} \right)^\top \\ &= \left(\frac{\bar{x}_{y-1}^l - x_i^l}{|\bar{x}_{y-1}^l - x_i^l|}, -1 \right)^\top, \end{aligned} \quad (2)$$

where \bar{x}_{y-1}^l is the mean x -coordinate of all points belonging to lane l in row $y-1$. This process is illustrated in Figure 2c, where pixels in green represent points belonging to lanes l . Note that unlike the HAF, unit vectors in the VAF point to the mean location of the lane in the previous row.

Decoding HAFs and VAFs: After a model is trained to predict the HAFs and VAFs detailed above, a decoding procedure is carried out to cluster foreground pixels into lanes during testing. This procedure is presented in Algorithm 2, and similarly operates row-by-row, from bottom to top.

Assuming $\vec{H}_{pred}(\cdot, \cdot)$ is the vector field corresponding to the predicted HAF, foreground pixels in a row $y-1$ are first assigned to clusters based on the following rule:

$$c_{haf}^*(x_i^{fg}, y-1) = \begin{cases} C^{k+1} & \text{if } \vec{H}_{pred}(x_{i-1}^{fg}, y-1)_0 \leq 0 \\ & \wedge \vec{H}_{pred}(x_i^{fg}, y-1)_0 > 0, \\ C^k & \text{otherwise,} \end{cases} \quad (3)$$

where $c_{haf}^*(x_i^{fg}, y-1)$ denotes the optimal cluster assignment for a foreground pixel $(x_i^{fg}, y-1)$; C^k and C^{k+1} denote two different clusters indexed by k and $k+1$ respectively. This assignment is illustrated in Figure 2b, where pixels in red are assigned the same cluster.

Next, these horizontal clusters are assigned to existing lanes indexed by l using the vector field $\vec{V}_{pred}(\cdot, \cdot)$ corresponding to the VAF as follows:

$$c_{vaf}^*(l) = \arg \min_{C^k} d^{C^k}(l), \quad (4)$$

where

$$d^*(l) = \min_{C^k} d^{C^k}(l). \quad (5)$$

Here $d^{C^k}(l)$ denotes the error of associating cluster C^k to an existing lane l :

$$\begin{aligned} d^{C^k}(l) &= \frac{1}{|C^k|} \sum_{i=0}^{|C^k|-1} \left\| (\bar{x}^{C^k}, y-1)^\top - (x_i^l, y)^\top \right. \\ &\quad \left. - \vec{V}_{pred}(x_i^l, y) \cdot \|(\bar{x}^{C^k}, y-1)^\top - (x_i^l, y)^\top\| \right\|. \end{aligned} \quad (6)$$

We illustrate this process in Figure 2d, where the cluster in red is assigned to the existing lane in green. By repeating the above steps row-by-row starting from the bottom and working to the top, we are able to assign every foreground pixel to their respective lanes.

C. Losses

To train the proposed model, we use a separate loss at each prediction head. For our binary segmentation branch, we used weighted binary cross-entropy loss, a standard loss for imbalanced binary segmentation tasks. The raw logits produced by the model are first passed through a sigmoid activation for normalization. The loss is then calculated as:

$$L_{BCE} = -\frac{1}{N} \sum_i \left[w \cdot t_i \cdot \log(o_i) + (1-t_i) \cdot \log(1-o_i) \right], \quad (7)$$

where t_i is the target value for the pixel i and o_i is the sigmoid output. Since this is an unbalanced segmentation task, a weight $w = 9.6$ was used to increase penalization for foreground pixels. To further account for the imbalanced dataset, an additional intersection over union loss was used for the segmentation branch:

$$L_{IoU} = \frac{1}{N} \sum_i \left[1 - \frac{t_i \cdot o_i}{t_i + o_i - t_i \cdot o_i} \right]. \quad (8)$$

For the affinity field branches of the model, a simple $L1$ regression loss was applied only to the foreground locations

TABLE I: Attributes of Lane Detection Datasets

Dataset	TuSimple	CULane
# Frames	6,408	133,325
Train	3,268	88,880
Validation	358	9,675
Test	2,782	34,680
Resolution	1280 × 720	1640 × 590
Road Type	highway	urban, rural, highway

of both the vertical and horizontal affinity fields:

$$L_{AF} = \frac{1}{N_{fg}} \sum_i \left[|t_i^{haf} - o_i^{haf}| + |t_i^{vaf} - o_i^{vaf}| \right]. \quad (9)$$

The total loss applied to the model is a simple summation of the individual losses:

$$L_{total} = L_{BCE} + L_{IoU} + L_{AF}. \quad (10)$$

IV. EXPERIMENTAL EVALUATION

A. Datasets

To train and benchmark our proposed approach, we make use of the popular TuSimple and CULane [20] datasets. TuSimple contains 3,626 annotated training video clips and 2,782 clips for testing. It features good and fair weather conditions in various daytime lighting and traffic conditions, employing highways with up to five lanes. Meanwhile, CULane contains significantly more data with 88,880 annotated training video clips and 34,680 clips for testing. This dataset also divides test images into nine categories and contains more complex scenarios, including images with challenging lighting conditions. A summary of both datasets is compiled in Table I.

B. Implementation Details

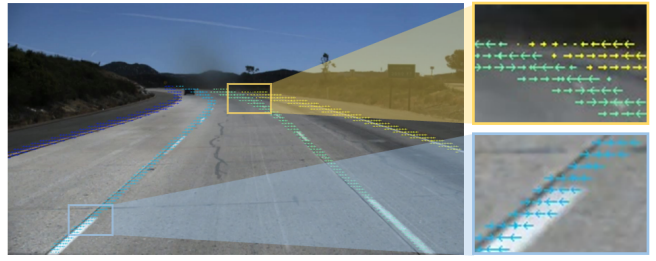
Our backbone architecture (DLA-34) is a fully convolutional network that does not retain the original resolution, but rather downsizes the outputs by a factor of 4; thus, we re-scaled the input images to 640×352 dynamically during run-time and also reshaped the ground truth affinity fields and segmentation masks to 160×88 , which is one quarter of the input size. This has the added benefit of making our decoding process faster since we now process only one quarter of the original rows. We also make use of random rotations, crops, scales and horizontal flips during training.

We use ImageNet pre-trained weights for the DLA-34 backbone and normalize the inputs accordingly. Finally, the Adam optimizer is used as our solver in all experiments. Other training parameters are listed below:

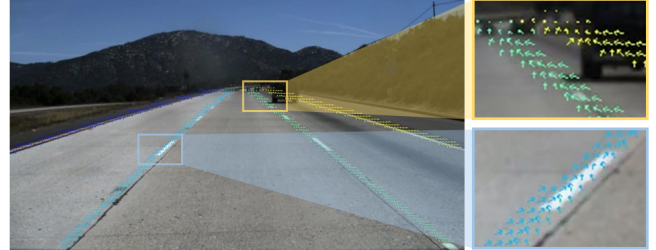
- Epochs = 60
- Batch size = 2
- Learning rate = $1e - 4$
- Weight decay = $1e - 3$

C. Metrics

We use the same evaluation metrics used in past literature to make a representative comparison between our approach and prior work. This consists of the official metric of the



(a) Predicted horizontal affinity field (HAF)



(b) Predicted vertical affinity field (VAF)

Fig. 3: Example outputs produced by LaneAF with color coded affinity fields; each color represents a unique lane instance based on affinity field decoding. Of note is the successful discrimination of lane instances even as the lanes converge.

TuSimple dataset (accuracy), the false positive (FP) rate, and the false negative (FN) rate. The TuSimple accuracy is calculated as:

$$Accuracy = \frac{N_{pred}}{N_{gt}} \quad (11)$$

where N_{pred} is the number of lane points that have been correctly predicted and N_{gt} is the number of ground-truth lane points. Additionally, we report the F1 measure, which is based on the intersection over union (IoU) and is the only metric for CULane. This is calculated as in [20]:

$$F1 = 2 \cdot \left(\frac{precision \cdot recall}{precision + recall} \right) \quad (12)$$

where $precision$ is defined as $\frac{TP}{TP+FP}$, $recall$ is defined as $\frac{TP}{TP+FN}$, TP is the number of lane points that have been correctly predicted, FP is the number of false positives, and FN is the number of false negatives.

D. Ablation Experiments

We conduct an ablation study to validate all our design choices. All ablation experiments were conducted on the TuSimple validation set and can be seen in Table II. The first row contains the results of the standard LaneAF model, which we denote as the baseline model B. First, we train variants without the IoU loss (B w/o IoU) and the weighted binary cross-entropy loss (B w/o wBCE). Removing these losses decreased accuracy quite drastically while increasing the false positive and false negative rate. In fact, without the weighted binary cross-entropy loss, the F1 score in particular

TABLE II: LaneAF Ablation Experiments on TuSimple for Validating Model Design

Model type	F1 (%)	Accuracy (%)	FP	FN
B ¹	95.31	94.62	0.0435	0.0500
B w/o IoU ²	95.17	94.31	0.0456	0.0507
B w/o wBCE ³	93.75	94.19	0.0598	0.0649
B w/o RT ⁴	93.56	94.29	0.0614	0.0670
B (DS-2) ⁵	94.76	94.22	0.0484	0.0559
B (DS-8)	93.94	92.73	0.0549	0.0656
B (HC-128) ⁶	94.80	94.56	0.0503	0.0535
DLA-34 multi-class ⁷	88.86	92.59	0.1115	0.1114

¹ B: baseline model with down-sampling factor 4 and 256 channels in output head ² IoU: IoU loss ³ wBCE: weighted BCE loss

⁴ RT: random transformations during training

⁵ DS-x: down-sampling factor for outputs

⁶ HC-x: number of channels in output head

⁷ DLA-34 multi-class: DLA-34 model trained for lane detection via multi-class segmentation

dropped significantly. The same is observed for the baseline model without random transformations during training (B w/o RT), as depicted in the fourth row.

With regards to the down-sampling factor of the outputs, it is clear that the baseline model’s factor of 4 achieved the best results; decreasing it to 2 (B (DS-2)) increased runtime and worsened accuracy and F1 slightly, while increasing it to 8 (B (DS-8)) had the most damaging effect on accuracy out of all modifications. We also trained a variant with 128 channels in the output head (B (HC-128)) compared to the original 256, and while this change had the smallest impact, it is evident that the baseline’s 256 channels yields superior results. Finally, to validate the benefits of our clustering approach over standard multi-class segmentation, we trained a DLA-34 model to directly perform multi-class segmentation of all lanes (DLA-34 multi-class). This model obtained the worst F1 and accuracy scores out of all variants. The result clearly illustrates the effectiveness of using binary segmentation and affinity field-based clustering as in our approach.

E. Results

Performance results from LaneAF on the TuSimple benchmark are shown in Table III. It can be seen that our false positive rate sets a new standard (0.0298) among the current state-of-the-art. This demonstrates that our model does not incorrectly detect a lane pixel as often as other networks and that LaneAF’s multi-branch approach leads to confident lane pixel predictions. While we obtain superior accuracy to other backbone architectures such as ResNet-18 and -34 [23], our approach falls slightly short of current state-of-the-art models such as PINet [15], ENet-SAD [12], and SCNN [20]. However, our false negative rate is only marginally higher, signifying that the incorrectly classified lane pixels are most likely at the very ends of the lanes.

Table IV displays the state-of-the-art results of our model on the CULane benchmark. With this significantly larger and more complex dataset, we can see that LaneAF’s performance improves greatly with respect to other models and demonstrates our network’s ability to generalize. LaneAF

TABLE III: LaneAF Results on the TuSimple Benchmark

Method	F1 (%)	Acc (%)	FP	FN	MACs (G)
SCNN [20]	96.53	96.53	0.0617	0.0180	-
ENet-SAD [12]	95.92	96.64	0.0602	0.0205	-
ResNet-18 [23]	87.87	92.69	0.0948	0.0822	-
ResNet-34 [23]	96.77	92.84	0.0918	0.0796	-
PINet [15]	97.20	96.75	0.0310	0.0250	-
LaneNet [13]	94.80	96.38	0.0780	0.0244	-
Cascaded-CNN [14]	90.82	95.24	0.1197	0.0620	-
PolyLaneNet [27]	90.62	93.36	0.0942	0.0933	1.7
LaneATT(ResNet-18) [21]	96.71	95.57	0.0356	0.0301	9.3
LaneATT (ResNet-34) [21]	96.77	95.63	0.0353	0.0292	18.0
LaneATT (ResNet-128) [21]	96.06	96.10	0.0564	0.0217	70.5
LaneAF (DLA-34)	96.42	95.64	0.0298	0.0413	17.5

outperforms the current state-of-the-art with an F1 score of 77.25%, surpassing models of similar size and even LaneATT with its largest backbone, ResNet-128. Moreover, LaneAF sets a new benchmark in a majority of categories, including difficult ones such as Dazzle, Shadow, Curve, and Night, exhibiting our model’s high adaptability to curving roads and challenging lighting conditions.

Qualitative results can be seen in Figures 3a and 3b. The clustered outputs shown here were created using the affinity field decoder, outlined in Algorithm 2. In Figure 3a, the HAF points towards the center of the lane line for each row of the output image. This is based on the valid lane pixels found in the binary segmentation output and represents the locations of potential lane instances with respect to all detected lane pixels. Lane clusters are still successfully separated despite their respective HAF being adjacent for numerous rows, demonstrated in yellow box of Figure 3a. Likewise, in Figure 3b, the VAF points along the lane towards the mean location of the next row’s lane pixels, which is based on the HAF outputs. This is visualized in the yellow box of Figure 3b, where for each unique lane instance, the unit vector points towards the next row’s mean lane pixel location. For both Figures 3a and 3b, the blue boxes clearly display how the HAF and VAF are implemented on a single detected lane instance.

In Figure 4, additional qualitative results are shown with samples from the TuSimple dataset in row 1 and the CULane dataset in rows 2-4. The TuSimple examples demonstrate LaneAF’s high performance on curved highways and on lanes that are merging and splitting due to entrances and exits, highlighting our model’s flexibility to the number of lanes present on a given road. Also notable in the middle image of the first row is the false detection of a lane line due to an airplane contrail. The displayed results from CULane include challenging scenarios that further illustrate LaneAF’s robustness on curved roads and in very poor lighting conditions. This diverse set of examples exhibit characteristics of the Dazzle, Shadow, Curve, and Night categories of the CULane dataset.

V. CONCLUDING REMARKS

In this paper, we proposed a novel approach to lane detection and instance segmentation through the use of binary segmentation masks and per-pixel affinity fields. The horizontal and vertical affinity fields, along with the predicted

TABLE IV: LaneAF State-of-the-Art Results on the CULane Benchmark

Method	Total	Normal	Crowded	Dazzle	Shadow	No line	Arrow	Curve	Cross	Night	MACs (G)
SCNN [20]	71.60	90.60	69.70	58.50	66.90	43.40	84.10	64.40	1990	66.10	-
ENet-SAD [12]	70.80	90.10	68.80	60.20	65.90	41.60	84.00	65.70	1998	66.00	-
Resnet-18 [23]	68.40	87.70	66.00	58.40	62.80	40.20	81.00	57.90	1743	62.10	-
Resnet-34 [23]	72.30	90.70	70.20	59.50	69.30	44.40	85.70	69.50	2037	66.70	-
PINet [15]	74.40	90.30	72.30	66.30	68.40	49.80	83.70	65.60	1427	67.70	-
SIM-CycleGAN [28]	73.90	91.80	71.80	66.40	76.20	46.10	87.80	67.10	2346	69.40	-
CurveLanes-NAS-M [29]	73.50	90.20	70.50	65.90	69.30	48.80	85.70	67.50	2359	68.20	33.7
LaneATT (ResNet-18) [21]	75.09	91.11	72.96	65.72	70.91	48.35	85.49	63.37	1170	68.95	9.3
LaneATT (ResNet-34) [21]	76.68	92.14	75.03	66.47	78.15	49.39	88.38	67.72	1330	70.72	18.0
LaneATT (ResNet-128) [21]	77.02	91.74	76.16	69.47	76.31	50.46	86.29	64.05	1264	70.81	70.5
LaneAF (DLA-34)	77.25	92.18	75.42	71.56	78.82	51.05	87.29	71.91	1500	72.69	18.6



Fig. 4: LaneAF qualitative results on TuSimple (row 1) and CULane (rows 2-4). The TuSimple examples demonstrate the model’s high performance on curved highways and on merging and splitting lanes. The challenging CULane scenarios further illustrate LaneAF’s robustness on curved roads and in a variety of poor lighting conditions.

binary masks were demonstrated to successfully cluster lane pixels into unique lane instances in a post-processing step. This is accomplished using a simple row-by-row decoding process with little overhead, and enables LaneAF to detect a variable number of lanes of arbitrary width without assuming a fixed or maximum number of lanes. This form of clustering is also more interpretable in comparison to previous visual approaches since it can be analyzed to easily identify and correct sources of error. The ablation study conducted also

validated the effectiveness of the approach over standard multi-class segmentation. Our proposed method achieves the lowest reported false positive rate (0.0298) on the TuSimple benchmark; on the larger and more comprehensive CULane dataset, LaneAF sets a new state-of-the-art result with a total F1 score of 77.25%, surpassing even much deeper and more complex models.

REFERENCES

- [1] M. Daily, S. Medasani, R. Behringer, and M. Trivedi, "Self-driving cars," *Computer*, vol. 50, no. 12, pp. 18–23, 2017.
- [2] N. Deo, A. Rangesh, and M. M. Trivedi, "How would surround vehicles move? a unified framework for maneuver classification and motion prediction," *IEEE Transactions on Intelligent Vehicles*, vol. 3, no. 2, pp. 129–140, 2018.
- [3] Z. Cao, T. Simon, S.-E. Wei, and Y. Sheikh, "Realtime multi-person 2d pose estimation using part affinity fields," in *Proceedings of the IEEE conference on computer vision and pattern recognition*, 2017, pp. 7291–7299.
- [4] K. Yuen and M. M. Trivedi, "Looking at hands in autonomous vehicles: A convnet approach using part affinity fields," *IEEE Transactions on Intelligent Vehicles*, vol. 5, no. 3, pp. 361–371, 2019.
- [5] F. Yu, D. Wang, E. Shelhamer, and T. Darrell, "Deep layer aggregation," in *Proceedings of the IEEE conference on computer vision and pattern recognition*, 2018, pp. 2403–2412.
- [6] A. Paszke, A. Chaurasia, S. Kim, and E. Culurciello, "Enet: A deep neural network architecture for real-time semantic segmentation," *arXiv preprint arXiv:1606.02147*, 2016.
- [7] R. K. Satzoda and M. M. Trivedi, "Drive analysis using vehicle dynamics and vision-based lane semantics," *IEEE Transactions on Intelligent Transportation Systems*, vol. 16, no. 1, pp. 9–18, 2014.
- [8] Q. Zou, H. Jiang, Q. Dai, Y. Yue, L. Chen, and Q. Wang, "Robust lane detection from continuous driving scenes using deep neural networks," *IEEE transactions on vehicular technology*, vol. 69, no. 1, pp. 41–54, 2019.
- [9] M. Ghafoorian, C. Nugteren, N. Baka, O. Booij, and M. Hofmann, "Elgan: Embedding loss driven generative adversarial networks for lane detection," in *Proceedings of the European Conference on Computer Vision (ECCV) Workshops*, 2018, pp. 0–0.
- [10] J. Phillion, "Fastdraw: Addressing the long tail of lane detection by adapting a sequential prediction network," in *Proceedings of the IEEE/CVF Conference on Computer Vision and Pattern Recognition*, 2019, pp. 11 582–11 591.
- [11] W. Van Gansbeke, B. De Brabandere, D. Neven, M. Proesmans, and L. Van Gool, "End-to-end lane detection through differentiable least-squares fitting," in *Proceedings of the IEEE/CVF International Conference on Computer Vision Workshops*, 2019, pp. 0–0.
- [12] Y. Hou, Z. Ma, C. Liu, and C. C. Loy, "Learning lightweight lane detection cnns by self attention distillation," in *Proceedings of the IEEE/CVF International Conference on Computer Vision*, 2019, pp. 1013–1021.
- [13] D. Neven, B. De Brabandere, S. Georgoulis, M. Proesmans, and L. Van Gool, "Towards end-to-end lane detection: an instance segmentation approach," in *2018 IEEE intelligent vehicles symposium (IV)*. IEEE, 2018, pp. 286–291.
- [14] F. Pizzati, M. Allodi, A. Barrera, and F. García, "Lane detection and classification using cascaded cnns," in *International Conference on Computer Aided Systems Theory*. Springer, 2019, pp. 95–103.
- [15] Y. Ko, J. Jun, D. Ko, and M. Jeon, "Key points estimation and point instance segmentation approach for lane detection," *arXiv preprint arXiv:2002.06604*, 2020.
- [16] T. Gupta, H. S. Sikchi, and D. Charkravarty, "Robust lane detection using multiple features," in *2018 IEEE Intelligent Vehicles Symposium (IV)*. IEEE, 2018, pp. 1470–1475.
- [17] N. Garnett, R. Cohen, T. Pe'er, R. Lahav, and D. Levi, "3d-lanenet: end-to-end 3d multiple lane detection," in *Proceedings of the IEEE/CVF International Conference on Computer Vision*, 2019, pp. 2921–2930.
- [18] Y. Huang, S. Chen, Y. Chen, Z. Jian, and N. Zheng, "Spatial-temporal based lane detection using deep learning," in *IFIP International conference on artificial Intelligence applications and innovations*. Springer, 2018, pp. 143–154.
- [19] R. K. Satzoda and M. M. Trivedi, "On enhancing lane estimation using contextual cues," *IEEE Transactions on Circuits and Systems for Video Technology*, vol. 25, no. 11, pp. 1870–1881, 2015.
- [20] X. Pan, J. Shi, P. Luo, X. Wang, and X. Tang, "Spatial as deep: Spatial cnn for traffic scene understanding," in *Proceedings of the AAAI Conference on Artificial Intelligence*, vol. 32, no. 1, 2018.
- [21] L. Tabelini, R. Berriel, T. M. Paixão, C. Badue, A. F. De Souza, and T. Oliveira-Santos, "Keep your eyes on the lane: Attention-guided lane detection," *Proceedings of the IEEE conference on computer vision and pattern recognition*, 2021.
- [22] M. Bai, G. Mattyus, N. Homayounfar, S. Wang, S. K. Lakshminanth, and R. Urtasun, "Deep multi-sensor lane detection," in *2018 IEEE/RSJ International Conference on Intelligent Robots and Systems (IROS)*. IEEE, 2018, pp. 3102–3109.
- [23] K. He, X. Zhang, S. Ren, and J. Sun, "Deep residual learning for image recognition," in *Proceedings of the IEEE conference on computer vision and pattern recognition*, 2016, pp. 770–778.
- [24] E. Romera, J. M. Alvarez, L. M. Bergasa, and R. Arroyo, "Erfnet: Efficient residual factorized convnet for real-time semantic segmentation," *IEEE Transactions on Intelligent Transportation Systems*, vol. 19, no. 1, pp. 263–272, 2017.
- [25] G. Huang, Z. Liu, L. Van Der Maaten, and K. Q. Weinberger, "Densely connected convolutional networks," in *Proceedings of the IEEE conference on computer vision and pattern recognition*, 2017, pp. 4700–4708.
- [26] J. Dai, H. Qi, Y. Xiong, Y. Li, G. Zhang, H. Hu, and Y. Wei, "Deformable convolutional networks," in *Proceedings of the IEEE international conference on computer vision*, 2017, pp. 764–773.
- [27] L. Tabelini, R. Berriel, T. M. Paixao, C. Badue, A. F. De Souza, and T. Oliveira-Santos, "Polylanenet: Lane estimation via deep polynomial regression," *arXiv preprint arXiv:2004.10924*, 2020.
- [28] T. Liu, Z. Chen, Y. Yang, Z. Wu, and H. Li, "Lane detection in low-light conditions using an efficient data enhancement: Light conditions style transfer," in *2020 IEEE Intelligent Vehicles Symposium (IV)*. IEEE, 2020, pp. 1394–1399.
- [29] Z. Li, "Curvelane-nas: Unifying lane-sensitive architecture search and adaptive point blending," in *Proceedings of the European Conference on Computer Vision (ECCV)*. Springer, 2020.